Atomically dispersed iron enables high-efficiency electrocatalytic conversion of nitrate to dinitrogen on a N-coordinated mesoporous carbon architecture

Jianwei Fan [a], Yanyan Chen [a], Xiaoqian Chen [a], Zhangxiong Wu [b], Wei Teng [a,*], Wei-xian Zhang [a]

[a] State Key Laboratory for Pollution Control, School of Environmental Science and Engineering, Shanghai Institute of Pollution Control and Ecological Security, Tongji University, Shanghai 200092, PR China
[b] Particle Engineering Laboratory, School of Chemical and Environmental Engineering, College of Chemistry, Chemical Engineering and Materials Science, Soochow University, Suzhou, Jiangsu 215123, PR China

ARTICLE INFO

ABSTRACT

Conversion of nitrate to dinitrogen (N_2) is a great challenge in environmental remediation, because it is difficult to control a complete N–N coupling reaction for N_2 generation. Herein, we report an atomically dispersed iron coordinated with nitrogen on an ordered mesoporous carbon framework (Meso-Fe–N–C) by a multicomponent co-assembly to improve the selectivity of electrocatalytic denitrification. Impressively, the N_2 conversion rate (2176 mg N h^{-1} g^{-1} Fe) is 1–3 orders of magnitude higher than that of other iron-based and previously reported materials. Both of N coordination and geometric distortion derived from mesostructure tune the electronic structure of Fe site. This leads to a modest adsorption binding strength with key intermediate to balance the amounts of the surface-bound and solvated nitric oxide (NO). Meanwhile, mesochannels confine solvated NO for dimerization via the Eley-Rideal mechanism to promote N_2 formation. The applicability over a wide pH range and long-term stability demonstrates potential practical application.

1. Introduction

Nitrogen cycle is an important part of the global biogeochemical cycle, but a serious imbalance of the nitrogen has been caused by intensified human activities, leading to a series of environmental problems [1,2]. One representative issue is the extensive eutrophication caused by the accumulation of toxic nitrogen oxyanions such as nitrate (NO_3^-) in surface and groundwater environments [3]. Nitrate waste also finds its way into drinking water. The excessive intake of nitrate in human can cause various diseases [4]. Therefore, selective reduction of nitrate to benign dinitrogen (N_2) is essential for ecological environment and human health. Compared with conventional biological denitrification, the electrocatalytic denitrification is considered as a promising technique thanks to the utilization of green electron as the reductant, its great resistance to fluctuation of water quality, and no secondary treatment [5–8]. Extensive research efforts have been made in direct conversion of NO_3^- to N_2 under mild pH conditions, but the formation of undesirable products such as ammonium/ammonia (NH_4^+/NH_3) makes it challenging to control a complete N–N coupling reaction for N_2 generation.

Nitric oxide (NO), the key intermediate, is regarded as the branched point to generate N_2 or NH_4^+/NH_3. Generally, for the electron-mediated denitrification, NO_3^- is firstly converted to nitrite (NO_2^-) and NO stepwise via oxygen deprivation [9]. Then one recognized pathway is that the surface-bound NO (*NO) is further reduced to dissociated nitrogen (*N), and once two *N combine, desired N_2 is formed (*N + *N → N_2) [10]. However, the N–N coupling reaction is rather difficult due to the high migration barrier of *N (0.75 eV) and advantageous kinetic competition of N–H bond formation [11]. Another favorable way is the dimerization of NO through the Eley-Rideal-like mechanism [1,12], whereby *NO reacts with solvated NO in solution to produce *N_2O which can be easily reduced to N_2. Thus, the increase of NO concentration and the balance of the surface-bound and solvated amounts of NO are critical for improving the N_2 yield. Therefore, it is reasonable to hypothesize that precise control of the catalyst architecture from microscopic electron distribution to macroscopic physical structure can regulate a moderate adsorption strength of NO on the active site followed by high-efficiency collision of NO for an enhanced selectivity of N_2.

Iron-based materials are environmentally-friendly catalysts with rich reserves, and have long been used for electrocatalysis [13–16]. The supported nanoscale zero-valent iron (nZVI) and Fe nanoparticles wrapped in N-doped carbon have been reported to develop for efficient electrocatalytic denitrification [17–19]. To further improve the catalytic conversion efficiency for N_2 generation, downsizing nanoparticles into atomically dispersed Fe anchored on matched supports should be a prospective strategy. As a frontier material, single-atom catalyst presents the following advantages: (i) the electronic structure of metal site can be properly tailored by its adjacent coordinative heteroatoms, thus enabling tunable bonding strength between intermediates and metal sites; (ii) the strong interaction between single atom and coordinative atom endows a long-term stability; (iii) the utmost atom utilization efficiency can boost the catalytic activity [20,21]. The other particularly important consideration is the selection of matched supports. Ordered mesoporous carbon as an excellent candidate offers a large surface area for high dispersion of active sites, proper and interconnected channels for diffusion of reactants, and good conductivity for facilitation of electron pathway [22,23]. More significantly, the interfacial curvature and confinement effect derived from the mesopores probably affect the reaction process [24–26].

Herein, the atomically dispersed iron coordinated with nitrogen on an ordered mesoporous carbon framework (Meso-Fe–N–C) was obtained by a multicomponent co-assembly method. The atomically dispersed Fe, N-coordination combined with the mesopore confinement enable an enhanced activity, stability, and especially selectivity for N_2 in electrocatalytic reduction of nitrate. The experimental and theoretical methods have been employed to investigate the structure-activity relationship and mechanism. Redistribution of the Fe electronic structure by both N coordination and the geometric distortion realizes the modest adsorption binding strength between the intermediate *NO and the Fe active site. Meanwhile, the confinement effect from mesopores facilities the dimerization between partially solvated NO and surface-bound NO to generate N_2. The catalyst exhibits long-term stability demonstrating its possibly practical application.

2. Experimental section

2.1. Preparation of Meso-Fe–N–C

The Meso-Fe–N–C catalysts were synthesized using a multicomponent co-assembly strategy. In a typical process, 3.2 g of F127 was dissolved in 30 mL ethanol with 20 mL of 0.2 M HCl and stirred at 40 °C. Next, 1.0 g of DCDA was added to obtain a clear solution A. After that, 0.3 g of $Fe(NO_3)_3 \cdot 9 H_2O$ dissolved in 10 mL ethanol was added dropwise into solution A to obtain solution B. Then, 4.16 g of TEOS and 10 g of 20 wt% resol solution (in ethanol) were added into solution B in sequence. After being stirred for 2 h, the above solution was transferred to Petri dishes and placed at room temperature for 12 h, and then heated at 100 °C for 24 h. The as-made products were pyrolyzed under an argon atmosphere at 350 °C for 2 h and then 800 °C for 2 h. The solid obtained was immersed into 2 M NaOH solution to remove the silica. The Meso-Fe–N–C powders were collected and dried after washing with DI water. The details about the reagents and chemicals, the processes for the preparation of Meso-N–C, Meso-FeNPs/C, Fe–N–C and nZVI are provided in supporting information (Text. S1–5).

2.2. Characterization

X-ray diffraction (XRD) patterns of catalysts were obtained using a D8 X-ray diffractometer equipped with Ni-filtered Cu Kα radiation (40 kV, 40 mA). The morphology of materials was characterized by high-resolution transmission electron microscopy (HRTEM, JEM-2100) and energy-dispersive X-ray spectroscopy (EDX). Atomic high-angle annular dark-field scanning transmission electron microscopy (HAADF-STEM) was conducted on an EM-ARM300F STEM with a spherical aberration

corrector. Nitrogen adsorption-desorption isotherms were measured at 77 K by Quantachrome Autosorb-iQ3 analyzer. The specific surface areas (S_{BET}) were calculated using Brunauer-Emmett-Teller method. X-ray photoelectron spectroscopy (XPS) analysis was carried out on a Thermo Scientific K-Alpha X-ray Photoelectron Spectrometer with Al Kα X-ray (hν = 1486.6 eV) radiation. Raman spectra was acquired from a Renishaw inVia Raman spectroscopy system with a 532 nm excitation laser. The Fe K-edge X-ray absorption fine structure (XAFS) spectra of Meso-Fe–N–C including X-ray absorption near-edge structure (XANES) and extended X-ray absorption fine structure (EXAFS) data was collected at the Beijing Synchrotron Irradiation Facility (BSRF, 1W1B) with stored electron energy of 2.2 GeV using transmission mode. The data of Fe K-edge spectra was processed using the IFEFFIT package. The iron content of catalysts was analyzed by dissolving the materials in aqua regia and testing iron content in the resulting solution through inductively coupled plasma optical emission spectrometry (ICP-OES, Agilent 5110). Iron leaching of catalysts after 24 h electrocatalytic nitrate reduction was also measured by inductively coupled plasma source mass spectrometer (ICP-MS, Agilent 7700).

2.3. Electrocatalytic denitrification

All the electrocatalytic nitrate reduction experiments were carried out on a CHI 660D electrochemical workstation (Shanghai Chenhua Instrument Co.) with a three-electrode electrochemical reaction cell (40 mL) at room temperature. A saturated calomel electrode and a platinum foil were used as the reference and counter electrodes, respectively. The working electrode was prepared as follows: 2.5 mg of catalyst, 0.3 mL of ethanol, 75 μL of Nafion (5 wt%) solution were mixed and sonicated for 30 min to form a uniform dispersion. Then, the above mixture was coated homogeneously onto a carbon paper (2 × 2 cm^2). During a typical electrocatalytic nitrate reduction experiment, a solution with a concentration of 50 mg L^{-1} of $NaNO_3$-N and 0.1 M of Na_2SO_4 was used as the electrolyte if not specially mentioned. The influences of various factors, including the initial concentration of NO_3N (15–100 mg L^{-1}), reaction time, cathode potential (from −1.2 to −1.5 V), and initial pH (4−10) on the denitrification performance of the Meso-Fe–N–C catalyst were investigated. The catalytic stability of Meso-Fe–N–C was also evaluated through cycling tests. The initial pH value of solution was adjusted by NaOH and H_2SO_4 solutions.

2.4. Electrochemical measurements

The LSV tests were performed on a system with different electrolytes and nitrate concentrations at a scan rate of 50 mV s^{-1}. The current-time (i-t) curves were recorded at a cathode potential of − 1.3 V vs. SCE for 24 h during the electrocatalytic nitrate reduction experiments. Rotating disk electrode (RDE) data was obtained using a Pine model MSRX rotator equipped with a Kel-F collet to hold the copper crystal on a CHI-760e electrochemical analyzer. The working electrode in the RDE tests was a glassy carbon disk (surface area = 0.19625 cm^{-2}) coated with Meso-Fe–N–C catalyst. The LSV curves under a series of rotating speeds were recorded at a scan rate of 10 mV s^{-1}.

2.5. In-situ differential electrochemical mass spectrometry (DEMS) measurements

The online-DEMS tests were carried on a Differential Electrochemical Mass Spectrometer (QAS100, Linglu Instruments (Shanghai) Co., Lt.). During the process, 50 mg L^{-1} of $NaNO_3$-N with 0.1 M Na_2SO_4 as electrolyte was flowed into a specially-made peristaltic pump-driven electrochemical cell. A Pt wire electrode, a saturated calomel electrode, and a carbon cloth covered with Meso-Fe–N–C powders were used as the counter electrode, the reference electrode, and the working electrode, respectively. The Ar gas was bubbled into the electrochemical device to assure a deoxygenated environment. After the baseline was

stable, the linear sweep voltammetry (LSV) tests were conducted from 0 to -1.4 V vs. SCE at a scan rate of 5 mV s^{-1} for four cycles. Each cycle started at the same test conditions after the mass signal returned to the baseline.

2.6. Analytical methods and data analysis

The concentrations of NO$_3$-N, NO$_2$-N, and NH$_4^+$-N were quantified by UV–vis spectrophotometer (DR-6000, Hach Co.). The intermediate nitrous oxides, such as N$_2$O, were negligible since they can be rapidly transformed to N$_2$ with excess hydrogen existed in the reaction system. Therefore, in our experiments, the generated gases were regarded as N$_2$. The nitrate removal efficiency was calculated by the equation:

$$R(100\%) = \frac{(C_0 - C_t)}{C_0} \times 100\%$$

Where C_0 and C_t (mg L^{-1}) refer to the initial NO$_3$-N concentration and the NO$_3$N concentration at time t, respectively.

The N$_2$ selectivity was estimated as the following equation:

$$S(100\%) = \frac{\Delta C(\text{NO}_3^--\text{N}) - \Delta C(\text{NO}_2^--\text{N}) - \Delta C(\text{NH}_4^+-\text{N})}{\Delta C(\text{NO}_3^--\text{N})} \times 100\%$$

Where $\Delta C(\text{NO}_3^--\text{N})$, $\Delta C(\text{NO}_2^--\text{N})$, and $\Delta C(\text{NH}_4^+-\text{N})$ represent the differences of NO$_3$-N, NO$_2$-N, and NH$_4^+$-N concentrations before and after electrocatalytic nitrate reduction, respectively.

More details about the analytical methods and data analysis, and DFT calculations are provided in the supporting information (Text. S6–7).

3. Results and discussion

3.1. Properties of the catalysts

The atomically dispersed iron coordinated with nitrogen on an ordered mesoporous carbon framework (denoted as Meso-Fe–N–C) was fabricated through a multicomponent co-assembly method (Fig. 1a). In the synthetic procedure, dicyandiamide (DCDA) reacts with the low-polymerized phenolic resins (resol, employed as the carbon precursor) by hydrogen bond or electronic attraction, and on the other hand, reacts with the Fe cations through amino chelation. The amphiphilic triblock polymer Pluronic F127 serves as the soft template for mesostructure assembly. Tetraethyl orthosilicate (TEOS) acts as the precursor to form a cross-linked silica network for a reinforced structure during the high temperature pyrolysis and further formation of interpenetrating micropores after NaOH leaching. The counterparts including Fe nanoparticles supported on mesoporous carbon (Meso-FeNPs/C), atomically dispersed Fe on N-doped carbon without mesoporous structure (Fe–N–C), N-doped mesoporous carbon without Fe addition (Meso-N–C) and nanoscale zero-valent iron (nZVI) particles were also prepared for comparison.
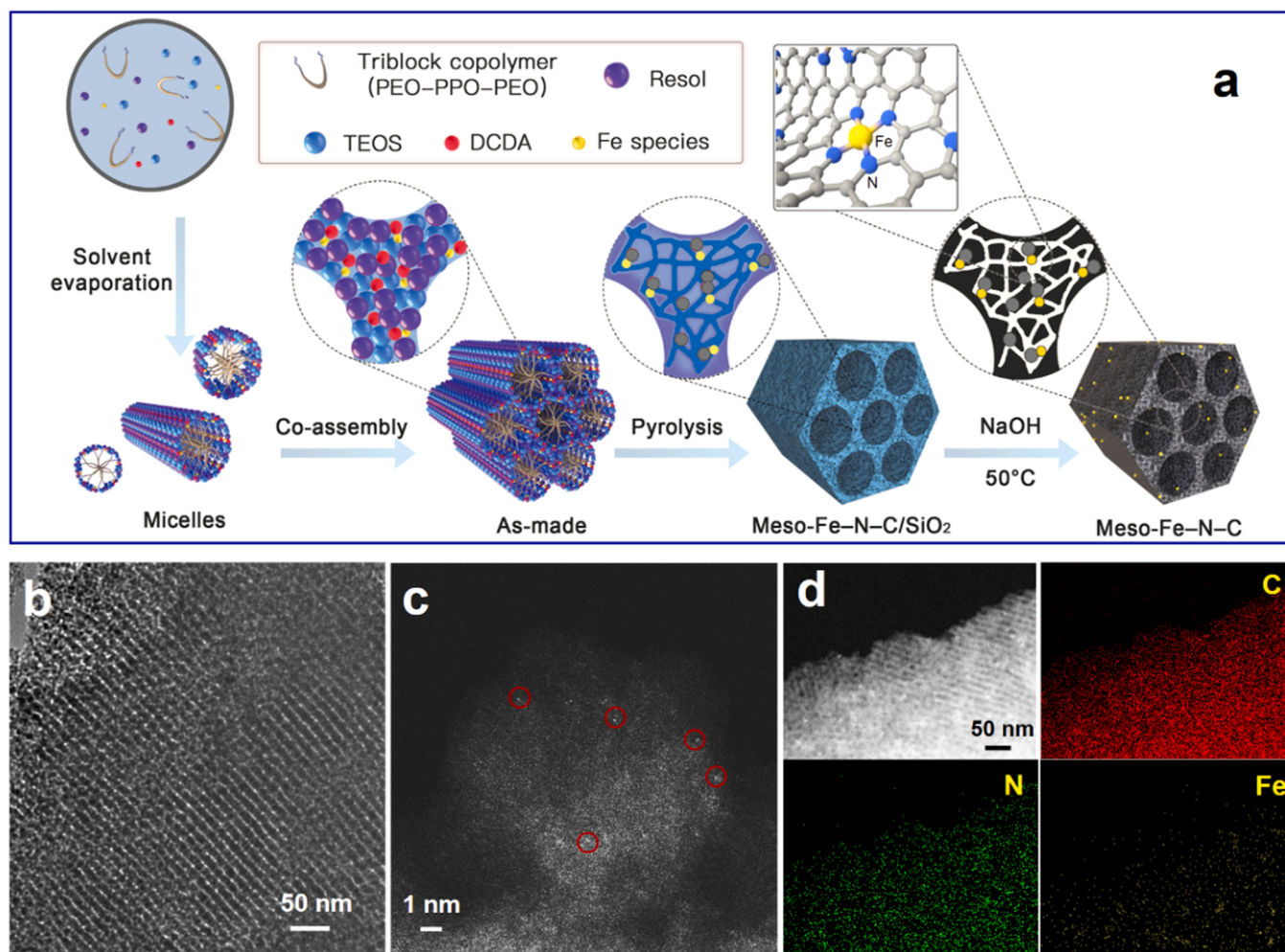

Fig. 1. (a) Schematic of synthetic procedures for atomically dispersed iron coordinated with nitrogen on an ordered mesoporous carbon framework (Meso-Fe–N–C) via a multicomponent co-assembly; (b) TEM image, (c) aberration-corrected high-angle annular dark-field scanning transmission electron microscopy (AC HAADF-STEM) image and (d) energy-dispersive X-ray (EDX) mappings of Meso-Fe–N–C.

The transmission electron microscopy (TEM) images of Meso-Fe–N–C (Fig. 1b) and other mesoporous materials (Figure. S1 and S2) show stripe-like arrangement with main pore sizes centered at 6–10 nm, confirming the ordered hexagonal mesostructure. Compared with Meso-FeNPs/C (Figure. S2), there are no aggregated nanoparticles can be observed across the whole frameworks of the Meso-Fe–N–C. Furthermore, the aberration-corrected high-angle annular dark-field scanning transmission electron microscopy (AC HAADF-STEM) was used to clearly reveal the Fe distribution at atomic resolution. As shown in Fig. 1c, the bright spots highlighted by the red circles can be identified to the Fe atoms. The same atomic dispersion is presented in the Fe–N–C sample (Figure. S3). Moreover, the energy-dispersive X-ray spectroscopy (EDX) mappings of Meso-Fe–N–C illustrate the homogeneous distribution of Fe and N species on the carbon frameworks (Fig. 1d).

The structural and textural properties of Meso-Fe–N–C were further demonstrated by small-angle X-ray scattering (SAXS) and N_2 sorption-desorption analysis. SAXS pattern (Figure. S4) of Meso-Fe–N–C clearly shows well-resolved scattering peaks, suggesting a highly ordered mesostructure with a two-dimensional (2D) hexagonal symmetry. The N_2 sorption-desorption isotherms of all the mesoporous composites show typical type-IV curves with distinct hysteresis loops, indicating the formation of mesoporous structures (Fig. 2a and S5). The surface area and the pore volume of Meso-Fe–N–C are up to 1010 $m^2\,g^{-1}$ and 1.2 cm^3 g^{-1}, respectively, much higher than that of most reported N-doped carbon supported Fe single atom or nanoparticles (Table. S1-2) [27–29]. This extraordinary property can offer abundant accessible active sites. The uniform bimodal mesopores centered at 9.1 and 2.0 nm are observed (Fig. 2a in set). The former mesopore caused by the soft template provides the main space for reaction, while the later left by removing the silica component connects the former mesopores for interpenetrated transport.

The wide-angle XRD pattern of Meso-Fe–N–C exhibits no additional peaks related to Fe species, and two broad and weak diffraction peaks at around 26° and 43° are assigned to the (002) and (101) of carbon structure, respectively (Fig. 2b). While Meso-FeNPs/C and nZVI exhibit typical peaks associated to Fe nanoparticles (Figure. S6, Text. S8). X-ray photoelectron spectroscopy (XPS) was taken to identify the surface chemical properties of the samples. The Fe 2p spectra of Meso-Fe–N–C can be fitted with Fe(II) and Fe(III), while the Fe(0) is observed in the Meso-FeNPs/C and nZVI samples (Figure. S7-9) [30]. The peaks of the N 1s spectra can be deconvoluted to five types of N species, in which the Fe-N_x peak (399.6 eV) confirms the coordination formation between Fe and N (Fig. 2c) [31]. The Fe contents of Meso-Fe–N–C (1.0 wt%) and other iron-based materials were quantified by inductively coupled plasma optical emission spectrometry (ICP-OES, Table. S3). The N content of Meso-Fe–N–C (2.0 wt%) was measured by elemental analysis (Table. S4).

X-ray absorption fine structure (XAFS) measurements were employed to further determine the coordinative structures of Meso-Fe–N–C (Table. S5). As shown in Fig. 2d, the X-ray absorption fine structure spectroscopy (XANES) spectrum of Meso-Fe–N–C displays the Fe K-pre-edge nearly close to that of iron phthalocyanine (FePc), demonstrating the atomic Fe–N–C structure [32]. The half-edge energy is between that of Fe_3O_4 and Fe_2O_3, indicating that the iron valence state in Meso-Fe–N–C is located between $+2$ and $+3$, in consistence with the XPS results [33]. The Fourier-transformed k^3-weighted extended X-ray absorption fine structure (EXAFS) spectrum of Meso-Fe–N–C shows the main peak at 1.5 Å, attributed to the Fe−N bond, and no Fe−Fe bond at 2.2 Å can be detected, thus implying the atomic dispersion of Fe on the matrix (Fig. 2e) [34]. The corresponding wavelet transform (WT) plot intuitionally exhibits maximum intensity at 5 $Å^{-1}$, assigned to Fe−N/O coordination (Figure. S10). Considered that the N precursor (DCDA) has no oxygen species, it can be inferred as atomic Fe–N–C structure rather than other Fe-derived compounds. The EXAFS curve of Meso-Fe–N–C fitting result for the first shell shows that each Fe atom is coordinated with ~4 N atoms with the average bond length of 2.01 Å (Fig. 2f and S11). The above results confirm that the atomic Fe–N_4 sites are highly dispersed on ordered mesoporous carbon architectures.
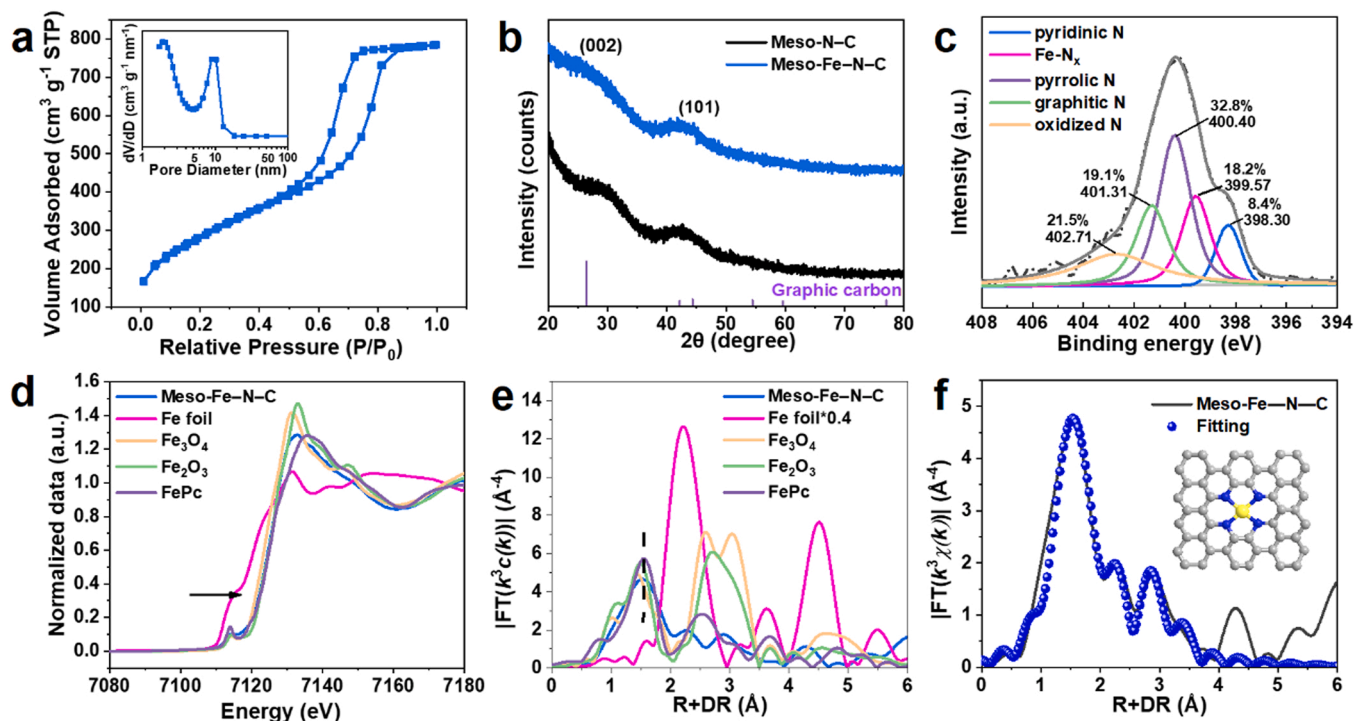

Fig. 2. (a) N_2 adsorption-desorption isotherms and the corresponding pore size distributions (an inset), (b) the wide-angle XRD pattern, and (c) high-resolution XPS spectrum of N 1 s of Meso-Fe–N–C. (d) Fe K-edge X-ray absorption near-edge structure (XANES) and (e) Fourier transform-extended X-ray absorption fine structure (FT-EXAFS) spectra of different samples. (f) EXAFS fitting of Meso-Fe–N–C (inset: model of FeN_4 site on the Meso-Fe–N–C. Fe yellow, N blue and C gray spheres).

3.2. Electrocatalytic denitrification performance

The electrocatalytic activities and N_2 selectivities of the nitrate reduction over Meso-Fe–N–C and its counterparts were investigated in a three-electrode system using a single-chamber cell (Fig. 3a). Meso-Fe–N–C shows the best denitrification performance with a nitrate removal of 77% and a N_2 selectivity of 85% in 0.1 M of Na_2SO_4 electrolyte. By contrast, Meso-N–C matrix without iron addition possesses poor performance with a nitrate removal of 36% and a N_2 selectivity of only 6%, indicating that the matrix contributes little to the denitrification. Furthermore, Fe nanoparticles supported on mesoporous carbon (Meso-FeNPs/C), Fe nanoparticles (nZVI) and Fe plate were employed for comparison. All the iron-based benchmark materials display inferior performances especially lower selectivities of N_2, implying that the Fe–N coordination of Meso-Fe–N–C should modulate the selectivity of the products. Significantly, the N_2 conversion ability of Meso-Fe–N–C is as high as 2176 mg N h^{-1} g^{-1} Fe, 3–1000 times higher than those of Meso-FeNPs/C, nZVI and previously reported iron-based catalysts (Fig. 3b-c, Table. S6) [18, 35, 37]. Moreover, the Fe–N–C material without a mesoporous structure was also compared. The lower activity (65%) and selectivity (66%) suggest the mesoporous confinement plays a favorable role in the denitrification.

The linear sweep voltammetry (LSV) curves of Meso-Fe–N–C in the presence and absence of nitrate in the electrolyte show a notable reduction peak at around − 0.46 V vs. SCE, implying the occurrence of nitrate electroreduction (Fig. 3d). Also, there is a weak nitrite reduction peak at about − 0.28 V vs. SCE when nitrite is added in the electrolyte. The nitrate reduction peak disappears at larger overpotential, probably because the reaction enters diffusive regime. In addition, the current density of Meso-Fe–N–C increases with the enhancement of nitrate concentration (Figure. S12).

The evolutions of nitrogen species over the Meso-Fe–N–C cathode were investigated during the electrocatalysis (Fig. 3e). The concentration of nitrate gradually decreases, achieving a removal rate of 77% within 24 h. During the process, nitrite was detected and its concentration increases at the first 2 h, followed by reducing to 0.3 mg N L^{-1},

implying that nitrite is an important intermediate product for conversion of nitrate to N_2. Meanwhile, the content of the final product NH_4^+ reaches the maximum at 5 h and then decreases to 10%, suggesting the partial oxidation of NH_4^+ to N_2 at the anode. The calculated selectivity of N_2 keeps increasing and eventually reaches 85%, demonstrating that predominant product is N_2.

The effects of various parameters including applied potential, pH of solution and initial nitrate concentration on the electrocatalytic performance of Meso-Fe–N–C were evaluated. The optimal performance is achieved at − 1.30 V vs. SCE (Fig. 4a), indicating that sufficient energy for nitrate reduction is obtained at this potential with little competition from HER. There is no obvious enhancement in the nitrate removal efficiency and N_2 selectivity at high potential (−1.50 V vs. SCE), probably due to the increasing competition of HER. Meso-Fe–N–C also exhibits almost unchanged N_2 selectivity (77–86%) between pH values of 4–10, confirming excellent applicability over a wide pH range (Fig. 4b). With the increase of initial nitrate concentration from 30 to 100 mg N L^{-1}, the nitrate removal efficiency decreased, but the nitrate removal capacity linearly elevates from 473 to 1028 mg N g^{-1} cat. (Fig. 4c-d). A low nitrate removal efficiency is obtained at an initial nitrate concentration of 15 mg N L^{-1}, which may be due to the reduced effective collision frequency of active molecules.

The Meso-Fe–N–C displays almost maintained nitrate conversion efficiency (65–74%) and N_2 selectivity (83–89%) during the six consecutive electrocatalytic reduction cycles (Fig. 3f). These results indicate a high electrocatalytic activity and stability of the catalyst. In each electrocatalysis, a near constant current density can be obtained within 24 h (Figure. S13), demonstrating an almost unchanged catalytic activity of Meso-Fe–N–C throughout the long-term reaction process. The leaching of iron ions is less than 0.1 wt% of total Fe content in Meso-Fe–N–C after each cycle test, which can be attributed to the strong interaction of metal-N coordination. XRD pattern and TEM image of the used Meso-Fe–N–C show that the structure and morphology maintained well (Figure. S14-15) after electrocatalytic reduction of nitrate. Besides, Fe-N_x species are unchanged after use according to the N 1s spectra of XPS (Figure. S16).
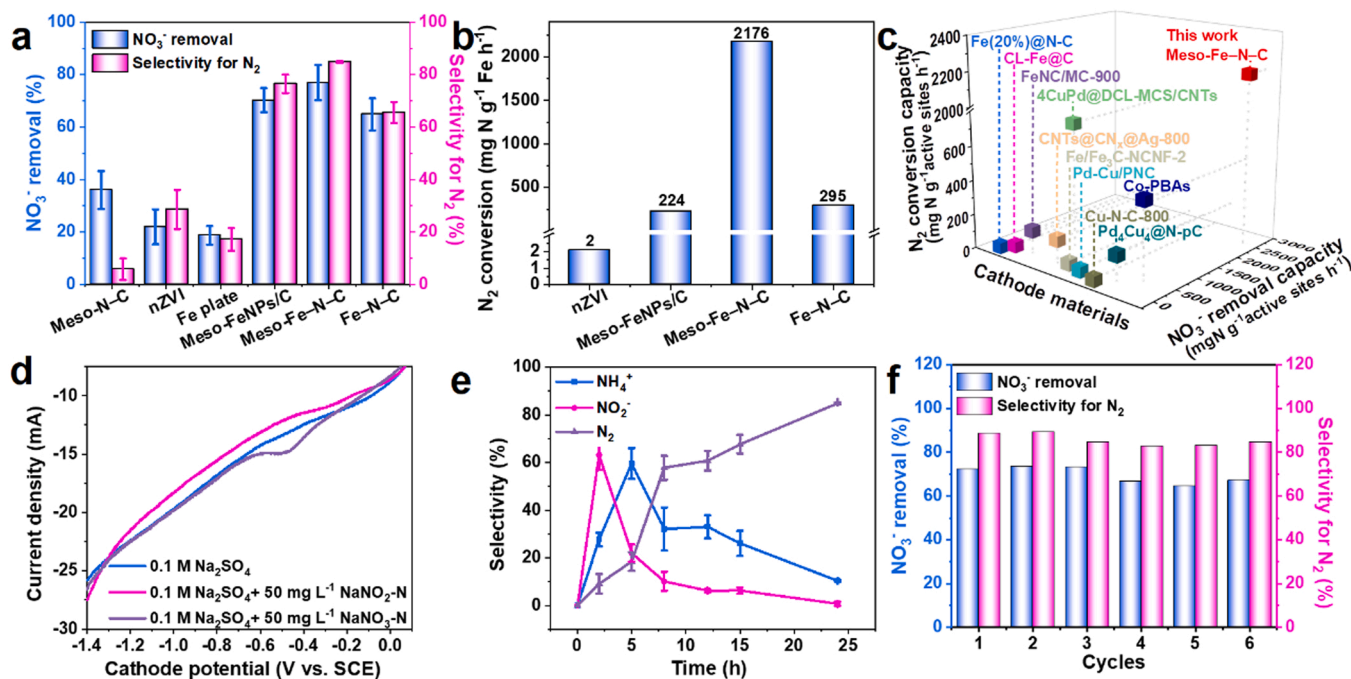

Fig. 3. (a) Nitrate removal efficiency and N_2 selectivity with different cathode materials. (b) N_2 conversion rate normalized to unit-mass of Fe. (c) Comparison of N_2 conversion and NO_3^- removal on unit active sites reported in literature. (d) LSV curves of Meso-Fe–N–C under different conditions. (e) Selectivity trends of different products over reaction time and (f) consecutive cycles for electrocatalytic denitrification over Meso-Fe–N–C (50 mg L^{-1} of NO_3-N, 40 mL, 0.1 M of Na_2SO_4, −1.3 V vs. SCE).
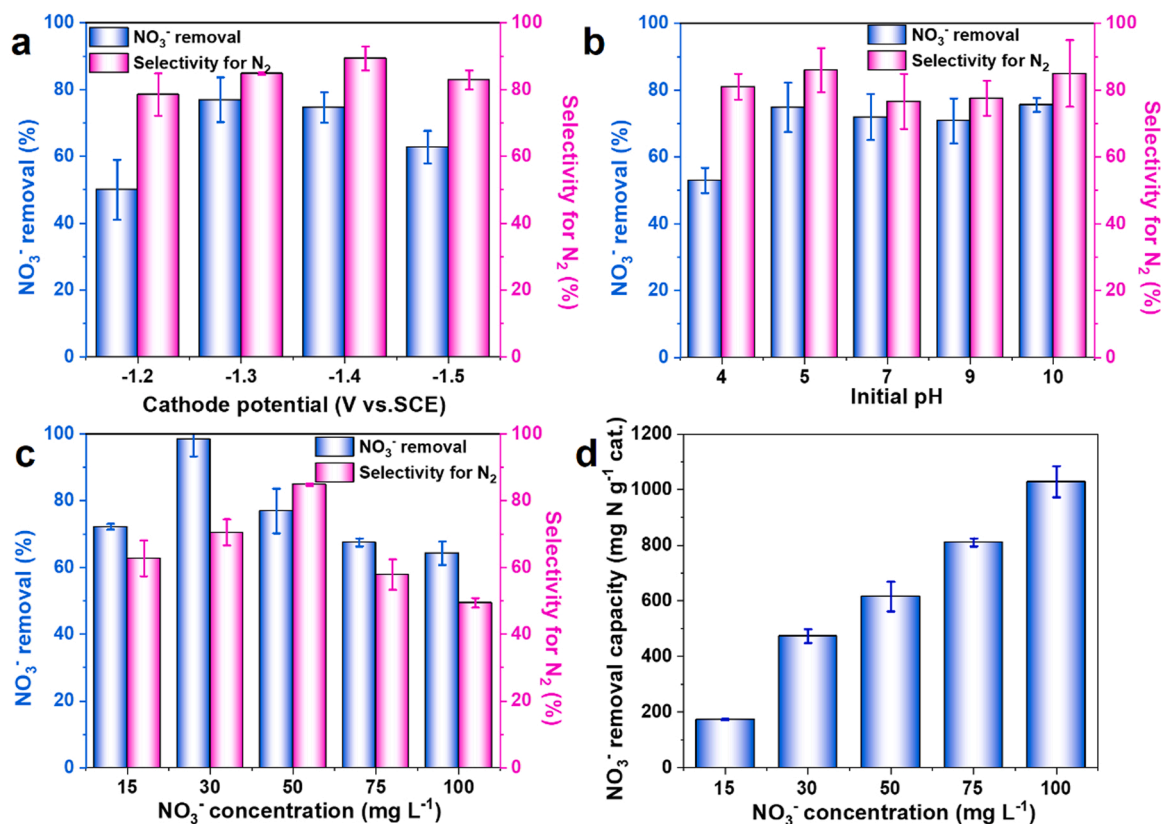
Fig. 4. Nitrate removal efficiency and selectivity for N_2 over Meso-Fe–N–C for electrocatalytic denitrification at different (a) voltages, (b) initial pH, (c) initial concentration of NO_3^--N, and (d) corresponding NO_3^- removal capacity over Meso-Fe–N–C at different initial concentration of NO_3^--N (50 mg L^{-1} of NO_3^--N, 40 mL, 0.1 M of Na_2SO_4, −1.3 V vs. SCE).

3.3. Proposed mechanism of electrocatalytic denitrification

The reaction pathway of electrocatalytic nitrate over Meso-Fe–N–C is investigated based on the linear sweep voltammograms (LSVs) collected on a rotating disk electrode (RDE) with 100–900 rpm (Fig. 5). Based on the Koutecky-Levich plots, the calculated electron transfer number (n) increases with the enhanced negative potential and reaches to 4.7 at −1.3 V vs. SCE, suggesting a main 5-electron process. The volatile nitrogen intermediates and products were detected during the electrocatalytic reduction of nitrate over Meso-Fe–N–C by online differential electrochemical mass spectrometry (DEMS, Fig. 6a). The m/z signals assigned to NO_2 (46), NO (30), N_2O (44), N_2 (28), NH_2OH (33), and NH_3

(17) appear repeatedly during the continuous four cycles in the potential region from 0 to −1.6 V vs. SCE. The strongest mass signal comes from $m/z = 28$, confirming that N_2 is the dominant product. The most probable pathway of nitrate reduction is elucidated depending on the signals: $NO_3 \rightarrow NO_2 \rightarrow NO \rightarrow N_2O \rightarrow N_2$.

Density functional theory (DFT) calculations were carried out for deeper insights into the selective denitrification mechanism on Meso-Fe–N–C. The free energy diagrams of electrochemical reduction of nitrate to N_2 via the 5-electron pathway and to NH_3/NH_4^+ via the 8-electron pathway over Meso-Fe–N–C and metallic Fe bulk are displayed in Fig. 6b and S17–18. The nitrate is firstly adsorbed on the surface Fe active sites ($*NO_3$), and then reduced to $*NO_2$ and $*NO$ in sequence by
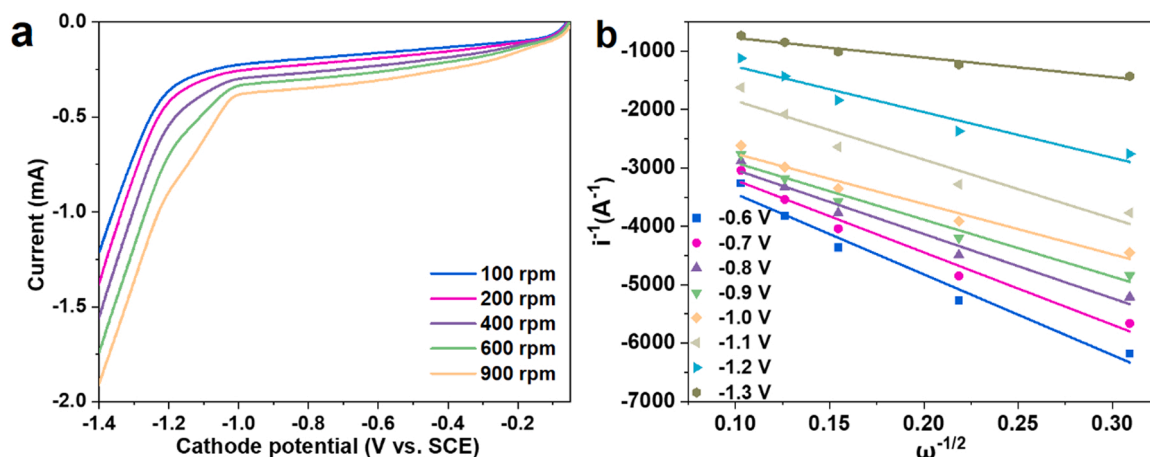

Fig. 5. (a) Rotating disk electrode voltammograms and (b) Koutecky-Levich plots obtained at different electrode potentials.
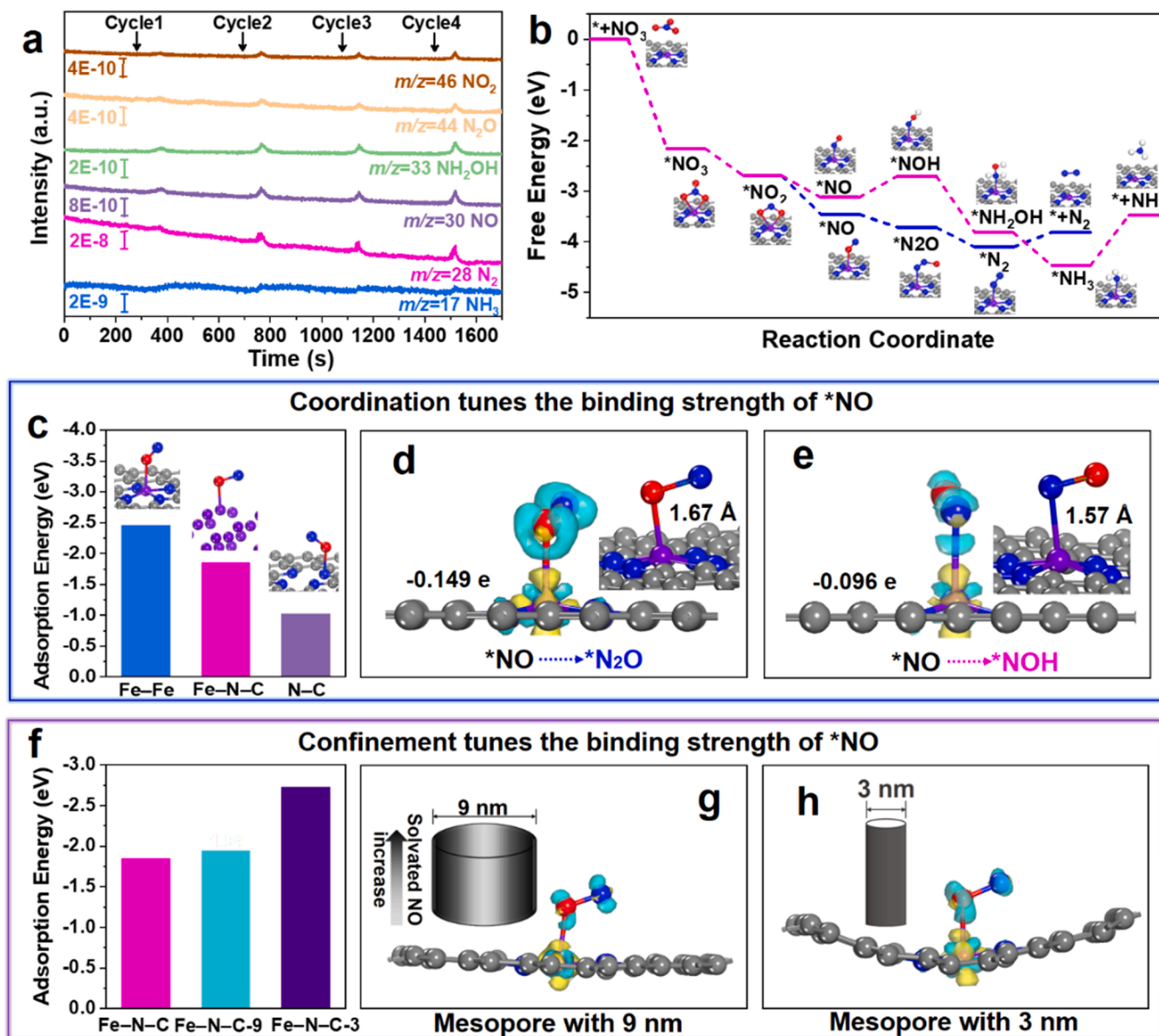
Fig. 6. (a) DEMS measurements of electrocatalytic denitrification over Meso-Fe–N–C in electrocatalytic NRR. (b) Free energy diagram of Meso-Fe–N–C. (c) Reaction energies of *NO adsorption on Fe bulk, Fe–N and N–C in Fe–N–C. Charge density difference diagrams of *NO on Fe–N–C in pathway of (d) N_2 generation (*NO to *N_2O) and (e) NH_3 formation(*NO to *NOH), and inset is corresponding elongation of the N–O bond diagrams. (f) Reaction energies and charge density difference diagrams of *NO adsorption on Fe–N–C-9 (Meso-Fe–N–C with 9 nm pore size) and Fe–N–C-3 with 3 nm pore size (g and h). Molecular model: N blue, O red, Fe purple, C gray.

cleavage of the N–O bond. The generated *NO as a branch is a key intermediate for the formation of N_2 or NH_3/NH_4^+ [38]. According to detected products from the DEMS and UV-Vis, one possible way is the reaction of surface-bound *NO with dissolved NO in solution (NO_{aq}) to produce the *N_2O through the dimerization process (Eley-Rideal-like reactions: *NO + NO_{aq} + 2 H^+ + 2e^- → *N_2O + H_2O) [7,12,39]. Then *N_2O can easily to be reduced to *N_2 and desorbed from the active sites [40]. The other way is successive hydrogenation of *NO to form *NOH, *NH_2OH, and finally the *NH_3 [41]. Notably, the Gibbs free energy differences for *N_2O generation [$\Delta G(*N_2O)$ = −0.30 eV] is much lower than *NOH generation process [$\Delta G(*NOH)$ = 0.41 eV], suggesting that 5-electron transfer for N_2 product is more thermodynamically favorable than 8-electron transfer for NH_3/NH_4^+ generation, well consistent with the experimental results. Besides, compared with Fe bulk, the lower energy state of every intermediate before the *N_2 formation over the Meso-Fe–N–C further demonstrates that the Fe–N active site is more

thermodynamically favorable than Fe–Fe site for N_2 emergence (Figure. S19).

The generation of ideal product N_2 is determined by a moderate binding strength of catalyst to balance the amounts of surface-bound NO and released NO for high-effective dimerization [38]. The adsorption energy of *NO (ΔE_{NO}) on Fe–Fe in metallic Fe bulk, and Fe–N and N–C in Fe–N–C were calculated based on DFT (Fig. 6c). The ΔE_{NO} value for Fe–N–C (−1.85 eV) is between that of Fe bulk and N–C, indicating a more appropriate binding strength for *NO. Different from the evenly distributed electron of Fe bulk and electronegative N in N–C, the Fe atom in Fe–N–C possesses a positive charge of 1.48e (Figure. S20), conducing to the adsorption and activation of *NO. Fig. 6d-e presents the electron density difference of *NO and Fe–N–C. Electropositive Fe prefers to bond with O atom of *NO for *N_2O generation, rather than *NOH generation by bonding with N atom. The more elongation of the N–O bond in the former case (1.67 Å, Fig. 6d inset) with significant charge redistribution

indicates the inclination of *N$_2$O transformation. Bader charge analysis confirms the number of transferred electrons from Fe–N–C to the *NO (−0.15e).

The confinement effect of mesoporous carbon, another significant factor conductive to the selective N$_2$ generation, is also considered and calculated. The effect mainly comes from the following two aspects. One is the geometry distortion of surface Fe–N–C active sites induced by the mesostructure [42,43]. To reveal the structure-activity relationship, the simplified models of graphene-type with different curvature were constructed (Figure. S21), including Fe–N–C confined in a planar graphene, and curved graphene with the diameter of 9 nm (based on the actual measurement, noted as Fe–N–C-9, equal to Meso-Fe–N–C) and 3 nm (simulated environment, noted as Fe–N–C-3). The Fe–N–C-9 displays slightly stronger binding strength for *NO adsorption (−1.94 eV) than flat Fe–N–C, but greatly weaker force than the Fe–N–C-3 (−2.73 eV), indicating that precise and optimal control the adsorption strength can be achieved by tuning the substrate distortion (Fig. 6f). The Mulliken charge of *NO further demonstrates moderate electron transfer over Fe–N–C-9 (−0.32e) to produce *N$_2$O via Eley-Rideal-like reactions (Fig. 6g-h). Additionally, slightly stronger adsorption ability of NO$_3^-$ on Fe–N–C-9 than that on planar Fe–N–C is benefit for the enhancement of reaction rate, in accord with the experimental results (Figure. S22). The other confinement effect from the mesopore is the changed distribution of NO concentration (Fig. 6g-h inset) [24]. Due to the appropriate binding with Meso-Fe–N–C, a portion of *NO is released from the active site but restricted in the nanoscale space with a diameter of 9 nm to avoid free diffusion. Thus, the concentration of solvated NO increases near by the active sites, resulting in the improvement of reaction probability between solvated and surface-bound *NO to form N$_2$O. On the contrary, for the planar Fe–N–C without confinement, the solvated NO randomly diffuses into the bulk solution with depressed encounter of *NO. This can explain why the N$_2$ selectivity of Fe–N–C is less than that of Meso-Fe–N–C.

Based on above experimental results and DFT calculations, the selective denitrification mechanism over Meso-Fe–N–C is probably as follows (Fig. 7). Firstly, due to the N coordination, Fe–N active sites are more thermodynamically favorable for electrochemical denitrification than Fe bulk. Meanwhile, the O-end adsorption structure between *NO and Meso-Fe–N–C provides moderate binding strength in favor of selective N$_2$ production via 5-electron pathway. Secondly, Mesostructure realizes the fine tuning of binding strength with *NO by changing the geometric distortion, conductive to the N$_2$ formation. Moreover, meso-channels confine solvated NO in a nanoscale space, leading to a greater

possibility for dimerization with *NO to generate N$_2$. According to above advantages, the atomically dispersed iron coordinated with nitrogen on an ordered mesoporous carbon framework exhibits excellent activity and selectivity for electrocatalytic reduction of nitrate.

According to previous reports, plenty of electrocatalytic denitrification mainly produce undesirable NH$_4^+$. Hence a strategy by adding extra chloridion (Cl$^-$) for ammonia oxidation through the active chlorine-mediated pathway is used to improve the N$_2$ selectivity [44,45]. This leads to the generation of toxic chlorinated byproducts which pose an additional threat to the environment [37]. In this work, only by precise design of commonly used iron from microscopic electronic structure to macroscopic physical structure, the novel architecture enables the improvement of the NO dimerization, and thus change the reduction reaction in a way that makes it more conducive to the formation of N$_2$. The sustainable service of the catalyst avoids chemical additives and extra risks.

4. Conclusions

In summary, a novel Fe single-atom catalyst coordinated with N on an ordered mesoporous carbon framework was prepared, exhibiting excellent electrocatalytic denitrification performance. Experimental and DFT calculation results demonstrate that N$_2$ generation via 5-electron transfer is the main nitrate reduction pathway. Notably, N$_2$ conversion rate (2176 mg N h^{-1} g^{-1} Fe) is one or even three orders of magnitude higher than that of other iron-based catalysts and previously reported active sites. The N coordination and mesoporous structure enable a modest adsorption binding strength between key intermediate *NO and Fe active site as well as a balance of amounts between the *NO and the solvated NO for enhanced N$_2$ formation. Our finding is a green strategy by design of a catalyst architecture from microscopic electron distribution to macroscopic structure for boosting the activity and selectivity of denitrification.

CRediT authorship contribution statement

Jianwei Fan: Methodology, Writing – original draft, Funding acquisition, Supervision. **Yanyan Chen:** Methodology, Software, Investigation, Formal analysis, Writing – original draft. **Xiaoqian Chen:** Methodology, Investigation. **Zhangxiong Wu:** Writing – review. **Wei Teng:** Concepts, Writing – original draft, Writing – review & editing, Funding acquisition, Supervision. **Wei-xian Zhang:** Writing – review , Supervision.
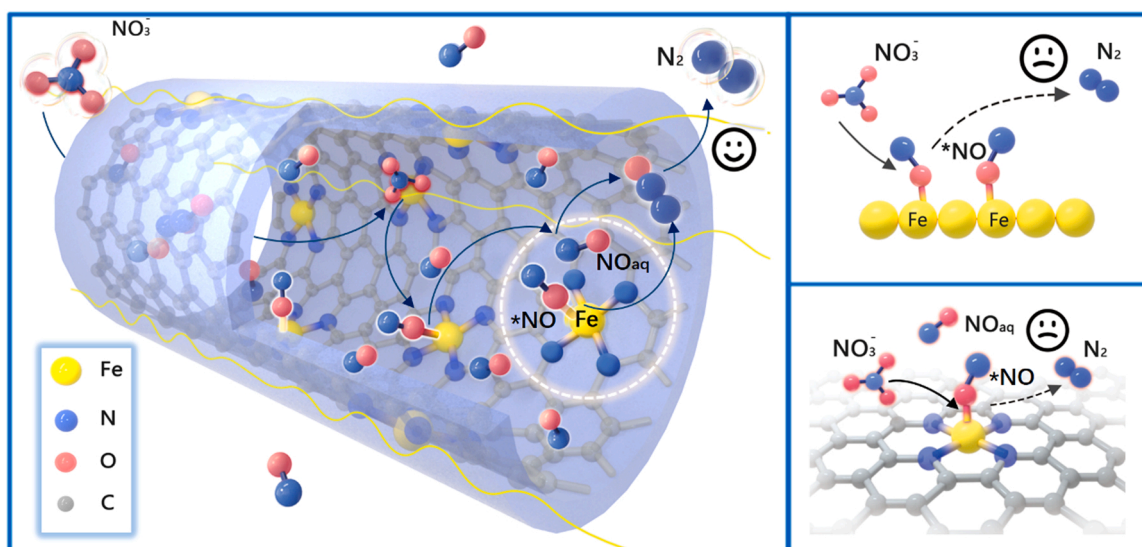
Fig. 7. Reaction mechanisms for electrocatalytic denitrification over (a) Meso-Fe–N–C, (b) metallic Fe bulk and (c) Fe–N–C without confinement.

Declaration of Competing Interest

The authors declare that they have no known competing financial interests or personal relationships that could have appeared to influence the work reported in this paper.

Data availability

Data will be made available on request.

Acknowledgments

Appendix A. Supporting information

Supplementary data associated with this article can be found in the online version at doi:10.1016/j.apcatb.2022.121983.

References

[1] V. Rosca, M. Duca, M.T. de Groot, M.T.M. Koper, Nitrogen cycle electrocatalysis, Chem. Rev. 109 (2009) 2209–2244, https://doi.org/10.1021/cr8003696.

[2] D.E. Canfield, A.N. Glazer, P.G. Falkowski, The evolution and future of Earth's nitrogen cycle, Science 330 (2010) 192–196, https://doi.org/10.1126/science.1186120.

[3] B.T. Nolan, B.C. Ruddy, K.J. Hitt, D.R. Helsel, Risk of nitrate in groundwaters of the United States-A national perspective, Environ. Sci. Technol. 31 (1997) 2229–2236, https://doi.org/10.1021/es960818d.

[4] A.M. Fan, V.E. Steinberg, Health implications of nitrate and nitrite in drinking water: an update on methemoglobinemia occurrence and reproductive and developmental toxicity, Regul. Toxicol. Pharmacol. 23 (1996) 35–43, https://doi.org/10.1006/rtph.1996.0006.

[5] M. Duca, M.T.M. Koper, Powering denitrification: the perspectives of electrocatalytic nitrate reduction, Energ. Environ. Sci. 5 (2012) 9726–9742, https://doi.org/10.1039/C2EE23062C.

[6] S. Garcia-Segura, M. Lanzarini-Lopes, K. Hristovski, P. Westerhoff, Electrocatalytic reduction of nitrate: fundamentals to full-scale water treatment applications, Appl. Catal. B 236 (2018) 546–568, https://doi.org/10.1016/j.apcatb.2018.05.041.

[7] Y. Wang, C. Wang, M. Li, Y. Yu, B. Zhang, Nitrate electroreduction: mechanism insight, in situ characterization, performance evaluation, and challenges, Chem. Soc. Rev. 50 (2021) 6720–6733, https://doi.org/10.1039/D1CS00116G.

[8] J. Sun, W. Gao, H. Fei, G. Zhao, Efficient and selective electrochemical reduction of nitrate to N2 by relay catalytic effects of Fe-Ni bimetallic sites on MOF-derived structure, Appl. Catal. B 301 (2022), 120829, https://doi.org/10.1016/j.apcatb.2021.120829.

[9] D. Sicsic, F. Balbaud-Célérier, B. Tribollet, Mechanism of nitric acid reduction and kinetic modelling, Eur. J. Inorg. Chem. 2014 (2014) 6174–6184, https://doi.org/10.1002/ejic.201402708.

[10] D. Xu, Y. Li, L. Yin, Y. Ji, J. Niu, Y. Yu, Electrochemical removal of nitrate in industrial wastewater, Front Environ. Sci. Eng. 12 (2018) 9, https://doi.org/10.1007/s11783-018-1033-z.

[11] J. Gao, B. Jiang, C. Ni, Y. Qi, X. Bi, Enhanced reduction of nitrate by noble metal-free electrocatalysis on P doped three-dimensional Co3O4 cathode: Mechanism exploration from both experimental and DFT studies, Chem. Eng. J. 382 (2020), 123034, https://doi.org/10.1016/j.cej.2019.123034.

[12] A. Clayborne, H. Chun, R.B. Rankin, J. Greeley, Elucidation of pathways for NO electroreduction on Pt(111) from first principles, Angew. Chem. Int. Ed. 54 (2015) 8255–8258, https://doi.org/10.1002/anie.201502104.

[13] J.A. Varnell, E.C.M. Tse, C.E. Schulz, T.T. Fister, R.T. Haasch, J. Timoshenko, A.I. Frenkel, A.A. Gewirth, Identification of carbon-encapsulated iron nanoparticles as active species in non-precious metal oxygen reduction catalysts, Nat. Commun. 7 (2016) 12582, https://doi.org/10.1038/ncomms12582.

[14] M. Lefèvre, E. Proietti, F. Jaouen, J. Dodelet, Iron-based catalysts with improved oxygen reduction activity in polymer electrolyte fuel cells, Science 324 (2009) 71–74, https://doi.org/10.1126/science.1170051.

[15] R. Sgarbi, K. Kumar, V.A. Saveleva, L. Dubau, R. Chattot, V. Martin, M. Mermoux, P. Bordet, P. Glatzel, E.A. Ticianelli, F. Jaouen, F. Maillard, Electrochemical transformation of Fe-N-C catalysts into iron oxides in alkaline medium and its impact on the oxygen reduction reaction activity, Appl. Catal. B 311 (2022), 121366, https://doi.org/10.1016/j.apcatb.2022.121366.

[16] Y. Jia, F. Zhang, Q. Liu, J. Yang, J. Xian, Y. Sun, Y. Li, G. Li, Single-atomic Fe anchored on hierarchically porous carbon frame for efficient oxygen reduction performance, Chin. Chem. Lett. 33 (2022) 1070–1073, https://doi.org/10.1016/j.cclet.2021.05.052.

[17] W. Teng, N. Bai, Y. Liu, Y. Liu, J. Fan, W. Zhang, Selective nitrate reduction to dinitrogen by electrocatalysis on nanoscale iron encapsulated in mesoporous carbon, Environ. Sci. Technol. 52 (2018) 230–236, https://doi.org/10.1021/acs.est.7b04775.

[18] W. Teng, J. Fan, W. Zhang, Iron-catalyzed selective denitrification over n-doped mesoporous carbon, ACS Appl. Mater. Interfaces 12 (2020) 28091–28099, https://doi.org/10.1021/acsami.0c03953.

[19] W. Duan, G. Li, Z. Lei, T. Zhu, Y. Xue, C. Wei, C. Feng, Highly active and durable carbon electrocatalyst for nitrate reduction reaction, Water Res 161 (2019) 126–135, https://doi.org/10.1016/j.watres.2019.05.104.

[20] A. Wang, J. Li, T. Zhang, Heterogeneous single-atom catalysis, Nat. Rev. Chem. 2 (2018) 65–81, https://doi.org/10.1038/s41570-018-0010-1.

[21] Y. Chen, S. Ji, C. Chen, Q. Peng, D. Wang, Y. Li, Single-atom catalysts: synthetic strategies and electrochemical applications, Joule 2 (2018) 1242–1264, https://doi.org/10.1016/j.joule.2018.06.019.

[22] W. Li, J. Liu, D. Zhao, Mesoporous materials for energy conversion and storage devices, Nat. Rev. Mater. 1 (2016) 16023, https://doi.org/10.1038/natrevmats.2016.23.

[23] Y. Meng, D. Gu, F. Zhang, Y. Shi, H. Yang, Z. Li, C. Yu, B. Tu, D. Zhao, Ordered mesoporous polymers and homologous carbon frameworks: amphiphilic surfactant templating and direct transformation, Angew. Chem. Int. Ed. 44 (2005) 7053–7059, https://doi.org/10.1002/anie.200501561.

[24] S. Zhang, M. Sun, T. Hedtke, A. Deshmukh, X. Zhou, S. Weon, M. Elimelech, J. Kim, Mechanism of heterogeneous fenton reaction kinetics enhancement under nanoscale spatial confinement, Environ. Sci. Technol. 54 (2020) 10868–10875, https://doi.org/10.1021/acs.est.0c02192.

[25] S. Zhang, T. Hedtke, X. Zhou, M. Elimelech, J. Kim, Environmental applications of engineered materials with nanoconfinement, ACS EST Engg 1 (2021) 706–724, https://doi.org/10.1021/acsestengg.1c00007.

[26] J. Qian, X. Gao, B. Pan, Nanoconfinement-mediated water treatment: from fundamental to application, Environ. Sci. Technol. 54 (2020) 8509–8526, https://doi.org/10.1021/acs.est.0c01065.

[27] Y. Gao, Y. Zhu, T. Li, Z. Chen, Q. Jiang, Z. Zhao, X. Liang, C. Hu, Unraveling the high-activity origin of single-atom iron catalysts for organic pollutant oxidation via peroxymonosulfate activation, Environ. Sci. Technol. 55 (2021) 8318–8328, https://doi.org/10.1021/acs.est.1c01131.

[28] W. Niu, L. Li, X. Liu, N. Wang, J. Liu, W. Zhou, Z. Tang, S. Chen, Mesoporous N-doped carbons prepared with thermally removable nanoparticle templates: an efficient electrocatalyst for oxygen reduction reaction, J. Am. Chem. Soc. 137 (2015) 5555–5562, https://doi.org/10.1021/jacs.5b02027.

[29] Y. Chen, Z. Li, Y. Zhu, D. Sun, X. Liu, L. Xu, Y. Tang, Atomic Fe dispersed on n-doped carbon hollow nanospheres for high-efficiency electrocatalytic oxygen reduction, Adv. Mater. 31 (2019) 1806312, https://doi.org/10.1002/adma.201806312.

[30] C. Cheng, S. Li, Y. Xia, L. Ma, C. Nie, C. Roth, A. Thomas, R. Haag, Atomic Fe-N-x coupled open-mesoporous carbon nanofibers for efficient and bioadaptable oxygen electrode in Mg-air batteries, Adv. Mater. 30 (2018) 1802669, https://doi.org/10.1002/adma.201802669.

[31] L. Jiao, G. Wan, R. Zhang, H. Zhou, S. Yu, H. Jiang, From metal-organic frameworks to single-atom Fe implanted n-doped porous carbons: efficient oxygen reduction in both alkaline and acidic media, Angew. Chem. Int. Ed. 57 (2018) 8525–8529, https://doi.org/10.1002/anie.201803262.

[32] Z. Zhang, J. Sun, F. Wang, L. Dai, Efficient oxygen reduction reaction (ORR) catalysts based on single iron atoms dispersed on a hierarchically structured porous carbon framework, Angew. Chem. Int. Ed. 57 (2018) 9038–9043, https://doi.org/10.1002/anie.201804958.

[33] K. Qian, H. Chen, W. Li, Z. Ao, Y. Wu, X. Guan, Single-atom Fe catalyst outperforms its homogeneous counterpart for activating peroxymonosulfate to achieve effective degradation of organic contaminants, Environ. Sci. Technol. 55 (2021) 7034–7043, https://doi.org/10.1021/acs.est.0c08805.

[34] L. Su, P. Wang, X. Ma, J. Wang, S. Zhan, Regulating local electron density of iron single sites by introducing nitrogen vacancies for efficient photo-fenton, Process, Angew. Chem. Int. Ed. 60 (2021) 21261–21266, https://doi.org/10.1002/anie.202108937.

[35] W. Duan, G. Li, Z. Lei, T. Zhu, Y. Xue, C. Wei, C. Feng, Highly active and durable carbon electrocatalyst for nitrate reduction reaction, Water Res 161 (2019) 126–135, https://doi.org/10.1016/j.watres.2019.05.104.

[36] L. Su, D. Han, G. Zhu, H. Xu, W. Luo, L. Wang, W. Jiang, A. Dong, J. Yang, Tailoring the assembly of iron nanoparticles in carbon microspheres toward high-performance electrocatalytic denitrification, Nano Lett. 19 (2019) 5423–5430, https://doi.org/10.1021/acs.nanolett.9b01925.

[37] B. Xu, Z. Chen, G. Zhang, Y. Wang, On-demand atomic hydrogen provision by exposing electron-rich cobalt sites in an open-framework structure toward superior electrocatalytic nitrate conversion to dinitrogen, Environ. Sci. Technol. 56 (2021) 614–623, https://doi.org/10.1021/acs.est.1c06091.

[38] T. Yoshioka, K. Iwase, S. Nakanishi, K. Hashimoto, K. Kamiya, Electrocatalytic reduction of nitrate to nitrous oxide by a copper-modified covalent triazine framework, J. Phys. Chem. C 120 (2016) 15729–15734, https://doi.org/10.1021/acs.jpcc.5b10962.

[39] A.C.A. de Vooys, M.T.M. Koper, R.A. van Santen, J.A.R. van Veen, Mechanistic study of the nitric oxide reduction on a polycrystalline platinum electrode, Electrochim. Acta 46 (2001) 923–930, https://doi.org/10.1016/S0013-4686(00)00678-2.

[40] J. Yang, M. Duca, K.J.P. Schouten, M.T.M. Koper, Formation of volatile products during nitrate reduction on a Sn-modified Pt electrode in acid solution,

J. Electroanal. Chem. 662 (2011) 87–92, https://doi.org/10.1016/j.jelechem.2011.03.015.

[41] Y. Wang, W. Zhou, R. Jia, Y. Yu, B. Zhang, Unveiling the activity origin of a copper-based electrocatalyst for selective nitrate reduction to ammonia, Angew. Chem. Int. Ed. 59 (2020) 5350–5354, https://doi.org/10.1002/anie.201915992.

[42] J. Yang, Z. Wang, C. Huang, Y. Zhang, Q. Zhang, C. Chen, J. Du, X. Zhou, Y. Zhang, H. Zhou, L. Wang, X. Zheng, L. Gu, L. Yang, Y. Wu, Compressive strain modulation of single iron sites on helical carbon support boosts electrocatalytic oxygen reduction, Angew. Chem. Int. Ed. 60 (2021) 22722–22728, https://doi.org/10.1002/anie.202109058.

[43] G. Han, X. Zhang, W. Liu, Q. Zhang, Z. Wang, J. Cheng, T. Yao, L. Gu, C. Du, Y. Gao, G. Yin, Substrate strain tunes operando geometric distortion and oxygen reduction activity of CuN2C2 single-atom sites, Nat. Commun. 12 (2021) 6335, https://doi.org/10.1038/s41467-021-26747-1.

[44] L. Su, K. Li, H. Zhang, M. Fan, D. Ying, T. Sun, Y. Wang, J. Jia, Electrochemical nitrate reduction by using a novel Co3O4/Ti cathode, Water Res 120 (2017) 1–11, https://doi.org/10.1016/j.watres.2017.04.069.

[45] X. Chen, T. Zhang, M. Kan, D. Song, J. Jia, Y. Zhao, X. Qian, Binderless and oxygen vacancies rich FeNi/graphitized mesoporous carbon/Ni foam for electrocatalytic reduction of nitrate, Environ. Sci. Technol. 54 (2020) 13344–13353, https://doi.org/10.1021/acs.est.0c05631.